NIH Public Access
Author Manuscript
Magn Reson Med. Author manuscript; available in PMC 2012 September 1.

Published in final edited form as:
Magn Reson Med. 2011 September ; 66(3): 831–838. doi:10.1002/mrm.22862.

Development of Chemical Exchange Saturation Transfer (CEST) at 7T

Adrienne N. Dula[1,2], **Elizabeth M. Asche**[3], **Bennett A. Landman**[1,2,3,4], **E. Brian Welch**[1,2], **Siddharama Pawate**[2,5], **Subramaniam Sriram**[5], **John C. Gore**[1,2,3], and **Seth A. Smith**[1,2,3]

[1] Department of Radiology and Radiological Sciences, Vanderbilt University, Nashville, TN USA

[2] Institute of Imaging Science, Vanderbilt University, Nashville, TN USA

[3] Department of Biomedical Engineering, Vanderbilt University, Nashville, TN USA

[4] Department of Electrical Engineering and Computer Science, Vanderbilt University, Nashville, TN USA

[5] Department of Neurology and Immunology, Vanderbilt University, Nashville, TN USA

Abstract

Chemical exchange saturation transfer (CEST) MRI is a molecular imaging method that has previously been successful at reporting variations in tissue protein and glycogen contents and pH. We have implemented Amide Proton Transfer (APT), a specific form of CEST imaging, at high field (7 Tesla) and used it to study healthy human subjects and patients with multiple sclerosis. The effects of static field inhomogeneities were mitigated using a water saturation shift referencing method to center each z-spectrum on a voxel-by-voxel basis. Contrary to results obtained at lower fields, APT imaging at 7 Tesla revealed significant contrast between white and gray matter, with a higher APT signal apparent within the white matter. Preliminary studies of multiple sclerosis showed the APT asymmetry varied with the type of lesion examined. An increase in APT asymmetry relative to healthy tissue was found in some lesions. These results indicate the potential utility of APT at high field as a non-invasive biomarker of white matter pathology, providing complementary information to other magnetic resonance imaging methods in current clinical use.

Keywords

Chemical exchange saturation transfer (CEST); amide proton transfer (APT); 7 Tesla; multiple sclerosis; white matter

INTRODUCTION

Magnetic resonance imaging (MRI) allows non-invasive examination of tissue properties *in vivo*, and conventional MRI (T1-, T2-weighted) produces excellent soft tissue contrast based on variations in tissue water content and macromolecular content, in both disease and health. Many pathologies are known to affect both tissue composition and water compartmentalization, but the former is difficult to assess by MRI because the proton populations in solid-like tissue components can in practice be detected only indirectly by their influence on the bulk water signal via magnetization transfer (MT). Most MT

Correspondence to: Adrienne N. Dula, Ph.D. 1161 21st Ave South AA-1101 MCN Nashville, TN 37232-2310 U.S.A. adrienne.n.dula@vanderbilt.edu Telephone: 615-343-0471 Fax: 615-322-0734 .

NIH-PA Author Manuscript
NIH-PA Author Manuscript
NIH-PA Author Manuscript

NIH-PA Author Manuscript

NIH-PA Author Manuscript

NIH-PA Author Manuscript

experiments are performed with saturation of the broad resonance of semi-solid like, macromolecular protons (characterized by short T2 on the order of microseconds) via one or many off-resonance (with respect to water) saturation prepulses prior to imaging (1). The saturated species is thought to interact with the magnetization of the bulk water compartment through direct chemical exchange or through-space dipole-dipole interactions, which reduces water signal. To assess the relation between the signal and the frequency of the saturating irradiation, a z-spectrum (2) is obtained. Typically the z-spectrum is broad (on the order of several kHz), shows little fine structure, and in tissues is found to be somewhat asymmetric (3,4).

Recently, a more specific and targeted MT technique has been devised to detect and measure particular exchangeable protons with relatively narrow resonances. This technique is termed chemical exchange saturation transfer (CEST) (5-7). Distinct from most MT imaging, the z-spectrum generated from off-resonance RF-irradiation shows a fine structure at the frequencies of specific exchanging species. When used to produce images, the contrast depends on the exchange rates and concentrations of specific chemical species whose resonant frequencies differ from water.

CEST MRI experiments are performed in a similar manner to MT MRI, but with important differences In MT imaging, the broad spectral lineshape of the semi-solid components can be saturated by a variety of short pulses, but in CEST imaging, in order to be sensitive to the resonances of interest, the RF irradiation bandwidth must be much more narrow. Using this approach, and by analyzing the asymmetry of the CEST spectrum, specific constituents such as amides and hydroxyl groups (8-11) may be quantified effectively creating an MRI-based molecular imaging method.

A practical drawback in CEST imaging is that the observed z-spectral asymmetry is very sensitive to the presence of magnetic field inhomogeneities, which can erroneously shift the center of the z-spectra. This may cause the minimum (i.e. point of maximum saturation) to occur at frequency offsets far from the water on-resonance reference frequency even in “well shimmed” situations. This confounding factor is further exacerbated at higher fields. One method to correct the center of the CEST spectra is to fit the CEST spectra to a polynomial (12) and find the minimum of the fit, which is deemed to be the reference frequency, and each voxel’s CEST spectrum may be shifted accordingly. However, the robustness of this technique relies on sampling the minimum of the CEST spectra in sufficient detail.

Recently, a separate acquisition with low saturation power, which detects the direct saturation of water, has been used to establish the frequency shift caused by field inhomogeneities and is termed water saturation shift referencing (WASSR) (13). With the WASSR technique, the direct water saturation spectrum is largely symmetric and directly reports the magnitude of the field inhomogeneities. This information then can be used to correct the center frequency of the subsequently obtained CEST acquisitions on a voxel-by-voxel basis. We have recently shown that the WASSR technique works robustly well at ultra-high field (7T) compared to B0 mapping for finding the center frequency of CEST data (ISMRM 2010, Stockholm, Sweden).

A particular feature of interest in CEST spectra are the amide protons which resonate around 3.5 ppm (10) off-resonance with respect to water. Analysis of these produces images that are termed amide proton transfer (APT)-weighted (APTw). APT imaging has been extensively studied *in vitro* (14,15), *in vivo* on animals (9,12), and *in vivo* in human subjects at 3T (8) and more recently at 7T (16). The APT asymmetry (APT_{asym}) has been shown to be of order

NIH-PA Author Manuscript

NIH-PA Author Manuscript

NIH-PA Author Manuscript

2-4% in some human pathological tissues at 3T (8,12) but significant contrast between different brain tissues has not been reported at lower field strengths.

Limitations of APT imaging include the low SNR and the small frequency offsets of the resonances of interest. However, migration of this technique to ultra-high field (7T) increases both the signal to noise ratio (SNR) and the spectral dispersion. We report here a preliminary study of CEST imaging at 7T that aims to evaluate the potential role of APT in characterizing neural tissues. In particular we have measured APT in normal brain as well as normal appearing white matter (NAWM), inflammatory lesions, and T1 holes in patients with multiple sclerosis (MS). These studies illustrate the potential of CEST methods for providing new information potentially relevant to the pathophysiology of demyelinating disease.

METHODS

MRI Experiments

Written informed consent was obtained from ten healthy control subjects (5 male, 5 female), age 32 ± 9 years (mean ± standard deviation) and four MS subjects (2 male, 2 female, 29 ± 6 years). All MRI studies were approved by our local institutional review board. All data were obtained on a Philips Achieva 7T scanner (Philips Healthcare, Cleveland, OH) equipped with a 16-channel NOVA head receiver coil (NOVA Medical, Wilmington, MA). The field was shimmed using 1^{st}, 2^{nd}, and 3^{rd} orders in all cases. The transmitted RF power was limited to a maximum of 3.2 W/kg resulting in a specific absorption rate well within the limit proposed by the Food and Drug Administration. Imaging volume and geometry were uniform for all scans: 8 slices were acquired (FOV = 212 × 212 × 24 mm^3, nominal resolution = 2.1 × 2.1 × 3.0 mm^3, reconstructed to 0.83 × 0.83 × 3.00 mm^3) covering the majority of the supratentorial cerebrum. CEST and WASSR images were acquired using a single-shot 3D turbo field echo (TFE) sequence. The saturation pulse used for WASSR imaging was 0.5 μT in amplitude, 200 ms in duration, and was swept between ± 1.0 ppm of resonance in increments of 0.08 ppm. For CEST, the saturation pulse (3.5 μT, 1000 ms) was swept between ± 7.0 ppm in 0.5 ppm increments. This CEST imaging was performed two times for accurate SNR calculations (17) resulting in a total CEST (13:55 minutes) and WASSR (5:00 minutes) scan time of 18:55 minutes. B0 maps were also obtained using the dual echo method (18) for comparison to the WASSR results. In addition, T2*-weighted (multi-echo fast field echo (FFE), TR/TE/ΔTE = 21/2.7/3.0 ms), T1-weighted MPRAGE (3D TFE, TR/TE = 3.7/1.98 ms, 1.0 × 1.0 × 3.0 mm^3, reconstructed to 0.83 × 0.83 × 3.00 mm^3), and a 3D FLAIR (3D Inversion recovery turbo spin echo, 1.0 mm^3 isotropic resolution, TR/TE/TI = 8000/344/2415 ms, as described by Zwanenburg et al. (19)) images were acquired on the patients with MS as well as selected controls. The specific imaging parameters are summarized in Table 1.

Processing

Image volumes were registered on a slice-by-slice basis using a mutual information algorithm written in Matlab (The Mathworks, Natick, MA). The T1-weighted anatomical images were used as the target for this slice-by-slice affine registration. The center frequency (so-called frequency shift maps) was measured using three techniques: WASSR (13), ΔB0 map calculation (18), and higher-order polynomial fit (12). The shift based on the polynomial fit was calculated by interpolating the CEST data to 100 points using piecewise cubic interpolation and fitting to a high order (25^{th} degree) polynomial. The global minima of the polynomial fits were determined for each pixel and used as the frequency shift.

NIH-PA Author Manuscript

NIH-PA Author Manuscript

NIH-PA Author Manuscript

The WASSR shift method for z-spectrum centering gave superior results in previous work, so this technique was implemented for all further analysis. The minimum of the WASSR spectrum was found using a maximum symmetry algorithm (13), producing a voxel-by-voxel frequency shift map. The WASSR shift was applied on a voxel-by-voxel basis to the normalized CEST data to create a centered CEST z-spectrum for each voxel. Asymmetry analysis was performed on these processed spectra and the CEST asymmetry ($CEST_{asym}$) for each pair of offsets was calculated:

$$CEST_{asym}(\Delta\omega) = \frac{S(-\Delta\omega) - S(\Delta\omega)}{S_o}, \quad [1]$$

where $\Delta\omega$ is the frequency offset of the saturation pulse, $S(\pm\Delta\omega)$ is the signal intensity at the positive and negative saturation offsets and S_o is the signal intensity without RF saturation. Of particular interest is the $CEST_{asym}$ at 3.5 ppm which has been shown to be sensitive to, though not exclusive to, the amide proton transfer and is termed amide proton transfer asymmetry (10).

Image Analysis

The amplitude of the calculated $CEST_{asym}$ (Eq. 1) at 3.5 ppm was defined as the APT_{asym} and was studied using region of interest (ROI) analyses of the z-spectra. All acquisitions were co-registered to the T1-weighted anatomical acquisition, so ROIs in the following structures were manually delineated on all T1-weighted images: corona radiata, genu and splenium of the corpus callosum, major and minor forceps, optic radiation, caudate, putamen, internal capsules, cerebrospinal fluid (CSF), and selected lesions (in the MS cases). The goal was to perform an analysis that could be easily applied to MS patients, so ROI analysis was chosen rather than segmentation. However, it is possible that the precise placement of ROIs could be a confounding factor and lead to inconsistent measurements and thus, the same set of ROIs were described by a second rater on all volunteers and the consistency of the measurements were assessed.

Statistics

The APT_{asym} for each ROI from each of two raters were compared in two ways. The mean APT_{asym} for each ROI through slices was calculated for each subject (n=10) and rater. Bland-Altman analysis was used to determine the variability between the two raters (20). This method tests if the 95% confidence interval (CI) of the difference between the two rater's measures includes zero. The limits of agreement (LOA) were also calculated to assess whether the difference falls outside the expected range. In addition, a non-parametric (Wilcoxon signed-rank) and parametric (paired *t*-test) were performed to test the difference between the two raters mean values ($\alpha = 0.01$).

Finally unpaired students *t*-tests were performed to test for differences among the APT_{asym} measured in healthy white matter (derived from controls), normal appearing white matter (MS), and T1 lesions (MS).

RESULTS

Anatomical, WASSR, and CEST imaging were successfully performed on all participants without any adverse events or significant image degradation due to motion artifacts. Figure 1A shows representative data acquired from a healthy subject at 7T. Figure 1C shows the ΔB0 map, figure 1D shows the result from a polynomial fit to the CEST data per voxel and figure 1E shoes the WASSR shift map. Compared to the polynomial fit, the WASSR method shows a more continuous and smooth range of data for the shift frequencies, and in

NIH-PA Author Manuscript

NIH-PA Author Manuscript

NIH-PA Author Manuscript

principle, the magnitude of the shift was higher than the ΔB0 map. Each of these methods were applied to the 7T CEST data and ROIs in the occipital white matter and genu of the corpus callosum were selected producing the CEST and asymmetry spectra Fig. 1A&B, respectively. The CEST spectra (solid lines, right y-axis), pre-shift (black), and those resulting from ΔB0 map (red), polynomial fit shift (blue), and WASSR shift (green), are shown along with the $CEST_{asym}$ (dashed lines, left y-axis) for each method of z-spectra correction in corresponding colors. The z-spectra were extrapolated back to the acquired offset frequencies following shifting, so the resulting spectra are under-sampled around the water resonance. The asymmetry analysis therefore focused on the offsets greater than 2 ppm, as demonstrated by the truncated $CEST_{asym}$ spectra in Fig. 1. The spectra arising from ROIs in the frontal and occipital white matter exhibit similar trends, although an increased inhomogeneity is expected in the frontal region of the image. The APT_{asym} maps resulting from each of the three different shift methods are shown in Fig. 1F-H. While in Figs. 1A&B, each method shows a similar degree of shift and resulting CEST spectra, it can be seen that the WASSR shift method results in a more robust, smoother APT_{asym} map (Fig. 1H) than does the APT_{asym} map derived from the ΔB0 shifting procedure. Additionally, in Figs 1G-H, considerable WM and GM contrast can be appreciated, which has not been previously reported at 7T (16) or 3T (8).

Fig. 2 shows the MPRAGE, FLAIR and CEST asymmetry results from a healthy control (A-C) and an MS subject (D-F), with ROI locations indicated by arrows. The FLAIR image shows a right, posterior, periventricular lesion in the MS subject (E) that is hypointense on the T1-weighted MPRAGE images. The corrected CEST spectra (solid lines) and asymmetry curves (dashed lines) from various ROIs are shown in Fig. 2G. Regional variations in WM APT_{asym} are seen in the spectra and in the APT_{asym} maps found in Fig. 2C and F (healthy and MS respectively) where WM APT_{asym} is seen to be higher than both GM and CSF (least APT_{asym}). The ROI placed within the CSF produces a symmetric Lorentzian CEST spectrum (cyan line, Fig. 2G) that likely is a reflection of the direct saturation effect (21). One point to note is that the NAWM from this MS subject exhibits increased asymmetry at the amide resonance (6.2%) relative to the healthy WM in the major forceps (4.8%).

The mean and standard deviation (over all healthy volunteers, n = 10) of APT_{asym} for each of 10 ROIs in WM, GM, and CSF were calculated and are shown in Figure 3. The error bars indicate the standard deviation among the 10 healthy subjects for each ROI. The vertical gray dashed line separates ROIs within the white matter from those in gray matter and CSF. A comprehensive analysis of healthy frontal WM exhibits an average asymmetry of (6.3 ± 0.7%) of the normalized signal at the amide resonance, which is elevated compared to the GM asymmetry (3.8 ± 0.5%). This difference has not previously been demonstrated using lower field strengths (12). Furthermore, we show that the APT_{asym} at 7T (16) is elevated in the corpus callosum.

Assessment of the consistency of these measurements was performed via intra-rater analysis. Bland-Altman analysis showed that the 95% confidence intervals for the mean difference between raters (D) overlaps zero in all cases, indicating there is no significant difference between the raters at the alpha = 0.05 level. In addition, neither the Wilcoxon signed-rank nor the paired *t*-test revealed significant differences between the raters ($p > 0.05$). The percent difference between raters (D_{BA}) also gives the reader an impression of the consistency of the data and was less than 4% for all measures except those taken in the optic radiation (12%) and the CSF (45%) which was expected due to the low APT_{asym} values obtained in the CSF. Detailed results of these statistical analyses can be found in Table 2.

NIH-PA Author Manuscript

NIH-PA Author Manuscript

NIH-PA Author Manuscript

The diversity of MS pathophysiology as well as the inconsistency of radiological findings complicates disease monitoring and prognosis. The contrast among T1-hypointense MS lesions, NAWM, and healthy WM is shown in Figure 2 but MS patients typically present with various lesion types. Figure 4 shows a different MS subject presenting with a heterogeneous periventricular lesion (Fig. 4A) with the posterior hypointense area indicated by the green arrow and the anterior hyperintense region indicated by the magenta arrow. The APT_{asym} map for this slice is shown in Fig. 4B, once again demonstrating the contrast between WM and GM but also highlighting areas of increased APT_{asym}. Fig. 4C shows the $CEST_{asym}$, corresponding to the right y-axis, and the APT_{asym}, corresponding to the left y-axis, of an ROI analysis of this particular periventricular lesion demonstrating its heterogeneity. The APT_{asym} was only 2.6 % in the hypointense, posterior area of the lesion (magenta) but 10.2 % in the anterior part of this lesion (green). Both of these are significantly different than that of the mean healthy control, 5.3 ± 1.0 %, ($p < 0.001$) using an unpaired *t*-test.

DISCUSSION

The results presented above demonstrate 1) the ability to perform WASSR corrected CEST imaging of the brain at 7T, and 2) the utility of CEST asymmetry analysis at 7T to examine both healthy and pathological tissue properties *in vivo*. Although migration of the established CEST techniques to higher field strengths for *in vivo* human application presents challenges, the sensitivity to field inhomogeneities was found to be mitigated with application of the WASSR method (13). As a first application, it was discovered that the WASSR method proved to be more consistent in centering the CEST spectra on a voxel-by-voxel basis than what was achieved with a B0 mapping approach and was relied on for the remainder of the analysis.

Analysis of the 7T APT_{asym}, reveals inherent differences among neural tissues that have not been seen at lower field strengths. These results were produced by choosing appropriate saturation pulse parameters based on previous experimental data (14) as well as establishing imaging parameters allowing a short acquisition time and sufficient resolution to avoid partial volume effects and maintain adequate SNR. This novel contrast may be apparent in ultra-high field imaging because of the increase in SNR and the use of smaller voxels that reduce partial volume effects. In addition, the prolonged T1 relaxation times at 7T result in slower recovery from saturation, which provides a lengthier time for sufficient exchange between proton pools.

In addition to the SNR advantages of higher fields, adequate spectral dispersion is also critical to achieve selective irradiation of the amide protons. The amides protons resonate at 3.5 ppm relative to water, which corresponds to 450 Hz at 3T. Creation of the CEST effect also produces some degree of direct saturation of the water, which may be higher at 3T due to the proximity of the amide and water resonances (8). At 7T, the offset of amide protons (1050 Hz) is further from the water resonance, reducing the saturation of the water. Additionally, we observed the width of the amide resonance to be approximately 0.5 ppm (corresponding to approximately 150 Hz) at full width at half maximum (FWHM). Assuming this is caused by variations in chemical shift and local field so that a similar FWHM of the same resonance arises at 3T, this would correspond to a spectral dispersion of the amide resonance of only 64 Hz, which could easily be missed. More studies need to be performed to ascertain the optimal duration of the CEST pulse (due to hardware limitations/RF droop) for extracting maximum signal from the amide resonance, and to explain the differences between the results at 7T and lower fields.

NIH-PA Author Manuscript

NIH-PA Author Manuscript

NIH-PA Author Manuscript

The analysis presented in Fig. 3 reveals a consistent difference in measured APT_{asym} among WM, GM, and CSF ROIs. The GM ROIs produced consistently lower APT_{asym} measurements. Although there are known potential confounding influences from conventional MT asymmetry, another plausible explanation for the apparent contrast in APT-weighted measures is that relative to WM, GM has fewer membrane-associated (extra-cellular, cytosolic and transmembrane) proteins such as those found in myelin and this potentially results in a lower concentration of exchangeable amide protons. It is interesting to consider the ramification of APT_{asym} sensitivity to endogenous proteins and peptides as related to one of the more prevalent neurological disorders, multiple sclerosis. While this study is preliminary and only reports on four MS subjects at 7T, the data suggest that there are distinct differences between the APT_{asym} measured in different lesion types. NAWM in MS is not normal, and is characterized by numerous signaling and adhesion proteins (22) as well as up-regulation of neuro-protective mechanisms, which are precursors to inflammatory-based disease activity (23) evident on conventional MRI scans (i.e. T1 and T2-weighted images). It has been suggested that some NAWM will go on to form lesions while other segments of NAWM will not, so the pathophysiology of NAWM remains difficult to interpret as a prognostic marker. However, examination of the elevated APT_{asym} seen in Fig. 2F & 2G may be related to these changes in the molecular composition of this tissue. With these key changes visible at 7T, it would be important to study a larger cohort to examine whether or not this is truly reflective of different (perhaps even temporally evolving) pathologies present in MS lesions.

It is also worth noting the differences between MS patients and healthy controls. We showed that APT_{asym} of NAWM was statistically different from that of healthy WM ($P < 0.001$). The literature has often pointed to so-called “dirty white matter” as seen on T2-weighted MRI, but otherwise, on conventional MRI, NAWM is often seen to be normal. One reason for this is that the lesions have not evolved to the point where inflammatory molecules and tissue edema are present. However, alternative strategies, such as MT, Diffusion Tensor Imaging-derived measures of anisotropy, and now CEST, report on the microenvironment, or specific macromolecular or protein components of tissue and are hypothesized to be less sensitive to inflammation. As a corroborative result, in Figure 4 the APT_{asym} demonstrates heterogeneity of the periventricular lesion, which is not apparent in the MPRAGE image. Additionally, lesions that are more chronic, (i.e appearing hypointense on the MPRAGE images) produced both APT_{asym} and CEST spectra that are similar to CSF. This is not unreasonable for chronic lesions, which are marked by tissue necrosis and thus this region is no longer rich in amide protons available for exchange (24,25). We hope that a further examination will reveal that CEST imaging applied to MS may hold potential for aiding in the determination/discrimination of MS lesion type.

Confidence in the sensitivity of the CEST asymmetry methods can be derived from previous studies performed on both animals as well as humans at lower field strengths. Animal studies at 4.7T have demonstrated differentiation of tumor core from surrounding edema (9,12) as well as higher APT_{asym} in the most solid-like regions of tumor (26). The ischemic penumbra may also be targeted with CEST (27). Human CEST experiments at 3T indicate pathological contrast can be established at lower field strengths in clinically applicable imaging times (8,26). This sensitivity is also demonstrated in the present study as shown in Figure 3 as well as the statistical analyses summarized in Table 2. The APT_{asym} metric has proven to be sensitive to tissue composition and demonstrates the ability to distinguish WM from GM and CSF when implemented at 7T.

Although confidence in these CEST-derived metrics has been established, interpretation of the results, particularly in the realm of pathology, is complicated. As such, it is important to note that any $CEST_{asym}$ value will depend on the power and duration of RF irradiation,

NIH-PA Author Manuscript

NIH-PA Author Manuscript

NIH-PA Author Manuscript

similar to conventional MT experiments, causing the results to differ with acquisition parameters as well as the manufacturer and coil used. Consequently as the impact of RF irradiation plays a roll in how much MT contributes (i.e. the magnitude of the so-called MT asymmetry) to the observed CEST-derived asymmetry, when implementing a CEST acquisition strategy, control data should always be obtained to compare with pathological cases. In addition, lipids resonate at a frequency opposite that of the amides in a range that is used as the reference for calculation of the APT_{asym}. Alteration in the lipid concentration or their exchange properties could affect the APT_{asym} measurements and must be considered when interpreting CEST spectra. Analysis of the reference side of the CEST spectrum (−2 to −4 ppm) could provide complementary information regarding tissue pathophysiology, particularly that of myelin within the white matter. Additional work is necessary to validate the opposite side of the CEST spectrum as an adequate reference, and additional characteristic methods (such as area of the amide resonance) need to be studied for their sensitivity and specificity compared to the analysis regimen presented here.

CONCLUSIONS

We have demonstrated the development and implementation of CEST MR imaging at 7T for the analysis of the APT_{asym} in healthy controls and we have shown preliminary analysis in a small cohort of patients with multiple sclerosis. Asymmetry between the positive and negative offset frequencies of the CEST spectra at the amide proton resonance (so-called APT_{asym}) shows contrast between white and gray matter in healthy tissue. Further, we showed that APT_{asym} is different between healthy volunteers and MS patients, and even within the MS cohort, reasonable differences were seen among lesions in different locations. Additionally, NAWM showed abnormal, yet elevated (contrary to the expected CEST effect in lesions visible on conventional MRI) APT_{asym} when compared to healthy control white matter. We suspect that a larger cohort will help in understanding these differences and based on preliminary results, we hypothesize that CEST imaging at 7T has the potential to become a noninvasive biomarker for white matter pathology. Furthermore, it can provide complementary information to existing MRI methods currently used in the clinic while possibly providing new insights regarding sub-clinical disease evolution.

Acknowledgments

The authors would like to acknowledge assistance from our technologists, Robin Avison, Donna Butler, Debbie Boner, and Leslie McIntosh for help with data acquisition and subject interaction. This work was supported by National Institutes of Health [grant number T32 EB001628 to J.G.] and [grant number EB009120 to S.S.].

ABBREVIATIONS

MT	magnetization transfer
CEST	chemical exchange saturation transfer
WASSR	water saturation shift referencing
APT	amide proton transfer
APTasym	amide proton transfer asymmetry
SNR	signal to noise ratio
NAWM	normal appearing white matter
MS	multiple sclerosis
FOV	field of view

NIH-PA Author Manuscript

NIH-PA Author Manuscript

NIH-PA Author Manuscript

TFE	turbo field echo
FFE	fast field echo
FLAIR	fluid attenuated inversion recovery
CESTasym	chemical exchange saturation transfer asymmetry
CSF	cerebrospinal fluid
WM	white matter
GM	gray matter
CI	confidence intervals
LOA	limits of agreement
D	mean difference
EPI	echo planar imaging.

References

1. Wolff SD, Balaban RS. Magnetization transfer contrast (MTC) and tissue water proton relaxation invivo. Magnetic Resonance in Medicine. 1989; 10(1):135–144. [PubMed: 2547135]
2. Bryant RG. The dynamics of water-protein interactions. Annual Review of Biophysics and Biomolecular Structure. 1996; 25:29–53.
3. Hua J, Jones CK, Blakeley J, Smith SA, van Zijl PCM, Zhou JY. Quantitative description of the asymmetry in magnetization transfer effects around the water resonance in the human brain. Magnetic Resonance in Medicine. 2007; 58(4):786–793. [PubMed: 17899597]
4. Pekar J, Jezzard P, Roberts DA, Leigh JS, Frank JA, McLaughlin AC. Perfusion imaging with compensation for asymmetric magnetization transfer effects. Magnetic Resonance in Medicine. 1996; 35(1):70–79. [PubMed: 8771024]
5. van Zijl PCM, Zhou J, Mori N, Payen JF, Wilson D, Mori S. Mechanism of magnetization transfer during on-resonance water saturation. A new approach to detect mobile proteins, peptides, and lipids. Magnetic Resonance in Medicine. 2003; 49(3):440–449. [PubMed: 12594746]
6. Ward KM, Aletras AH, Balaban RS. A new class of contrast agents for MRI based on proton chemical exchange dependent saturation transfer (CEST). Journal of Magnetic Resonance. 2000; 143(1):79–87. [PubMed: 10698648]
7. Wolff SD, Balaban RS. NMR imaging of labile proton-exchange. Journal of Magnetic Resonance. 1990; 86(1):164–169.
8. Jones CK, Schlosser MJ, van Zijl PCM, Pomper MG, Golay X, Zhou JY. Amide proton transfer imaging of human brain tumors at 3T. Magnetic Resonance in Medicine. 2006; 56(3):585–592. [PubMed: 16892186]
9. Salhotra A, Lal B, Laterra J, Sun PZ, van Zijl PCM, Zhou JY. Amide proton transfer imaging of 9L gliosarcoma and human glioblastoma xenografts. NMR in Biomedicine. 2008; 21(5):489–497. [PubMed: 17924591]
10. Zhou JY, Payen JF, Wilson DA, Traystman RJ, van Zijl PCM. Using the amide proton signals of intracellular proteins and peptides to detect pH effects in MRI. Nature Medicine. 2003; 9(8):1085–1090.
11. van Zijl PCM, Jones CK, Ren J, Malloy CR, Sherry AD. MRI detection of glycogen in vivo by using chemical exchange saturation transfer imaging (GLYCOCEST). Proceedings of the National Academy of Sciences, USA. 2007; 104(11):4359–4364.
12. Zhou JY, Lal B, Wilson DA, Laterra J, van Zijl PCM. Amide proton transfer (APT) contrast for imaging of brain tumors. Magnetic Resonance in Medicine. 2003; 50(6):1120–1126. [PubMed: 14648559]

NIH-PA Author Manuscript

NIH-PA Author Manuscript

NIH-PA Author Manuscript

13. Kim M, Gillen J, Landman BA, Zhou JY, van Zijl PCM. Water saturation shift referencing (WASSR) for chemical exchange saturation transfer (CEST) experiments. Magnetic Resonance in Medicine. 2009; 61(6):1441–1450. [PubMed: 19358232]

14. Sun PZ, van Zijl PCM, Zhou JY. Optimization of the irradiation power in chemical exchange dependent saturation transfer experiments. Journal of Magnetic Resonance. 2005; 175(2):193–200. [PubMed: 15893487]

15. Zhou JY, van Zijl PCM. Chemical exchange saturation transfer imaging and spectroscopy. Progress in Nuclear Magnetic Resonance Spectroscopy. 2006; 48(2-3):109–136.

16. Mougin OE, Coxon RC, Pitiot A, Gowland PA. Magnetization transfer phenomenon in the human brain at 7 T. NeuroImage. 2010; 49:272–281. [PubMed: 19683581]

17. Ohliger MA, Grant AK, Sodickson DK. Ultimate intrinsic signal-to-noise ratio for parallel MRI: electromagnetic field considerations. Magnetic Resonance in Medicine. 2003; 50:1018–1030. [PubMed: 14587013]

18. Skinner TE, Glover GH. An extended two-point dixon algorithm for calculating separate water, fat, and B0 images. Magnetic Resonance in Medicine. 1997; 37(4):628–630. [PubMed: 9094088]

19. Zwanenburg JJ, Hendriskse J, Visser F, Takahara T, Luijten PR. Fluid attenuated inversion recovery (FLAIR) MRI at 7.0 Tesla: comparison with 1.5 and 3.0 Tesla. European Radiology. 2009; 20(4):915–22. [PubMed: 19802613]

20. Bland JM, Altman DG. Statistical-methods for assessing agreement between 2 methods of clinical measurement. Lancet. 1986; 1(8476):307–310. [PubMed: 2868172]

21. Mulkern RV, Williams ML. The general-solution to the Bloch equation with constant RF and relaxation terms - Application to saturation and slice selection. Medical Physics. 1993; 20(1):5–13. [PubMed: 8455512]

22. Agrawal SM, Yong VW. Immunopathogenesis of multiple sclerosis. Neurobiology of Multiple Sclerosis. 2007; 79:99.

23. Lazzarini, RA. Myelin Biology and Disorders. Lazzarini, RA.; Griffin, JW.; Lassman, H.; Nave, K.; Miller, RH.; Trapp, BD., editors. Elsevier; Amsterdam, Boston, Heidelberg, London, New York, Oxford, Paris, San Diego, San Francisco, Singapore, Sydney, Tokyo: 2004.

24. Bruck W, Bitsch A, Kolenda H, Bruck Y, Stiefel M, Lassmann H. Inflammatory central nervous system demyelination: Correlation of magnetic resonance imaging findings with lesion pathology. Annals of Neurology. 1997; 42(5):783–793. [PubMed: 9392578]

25. van Walderveen MAA, Kamphorst W, Scheltens P, van Waesberghe JHTM, Ravid R, Valk J, Polman CH, Barkhof F. Histopathologic correlate of hypointense lesions on T1-weighted spin-echo MRI in multiple sclerosis. Neurology. 1998; 50(5):1282–1288. [PubMed: 9595975]

26. Zhou JY, Blakeley JO, Hua J, Kim M, Laterra J, Pomper MG, van Zijl PCM. Practical data acquisition method for human brain tumor amide proton transfer (APT) imaging. Magnetic Resonance in Medicine. 2008; 60(4):842–849. [PubMed: 18816868]

27. Sun PZ, Zhou J, Sun W, Huang J, van Zijl PCM. Detection of the ischemic penumbra using pH-weighted MRI. J Cereb Blood Flow Metab. 2007; 27(6):1129–36. [PubMed: 17133226]

NIH-PA Author Manuscript
NIH-PA Author Manuscript
NIH-PA Author Manuscript

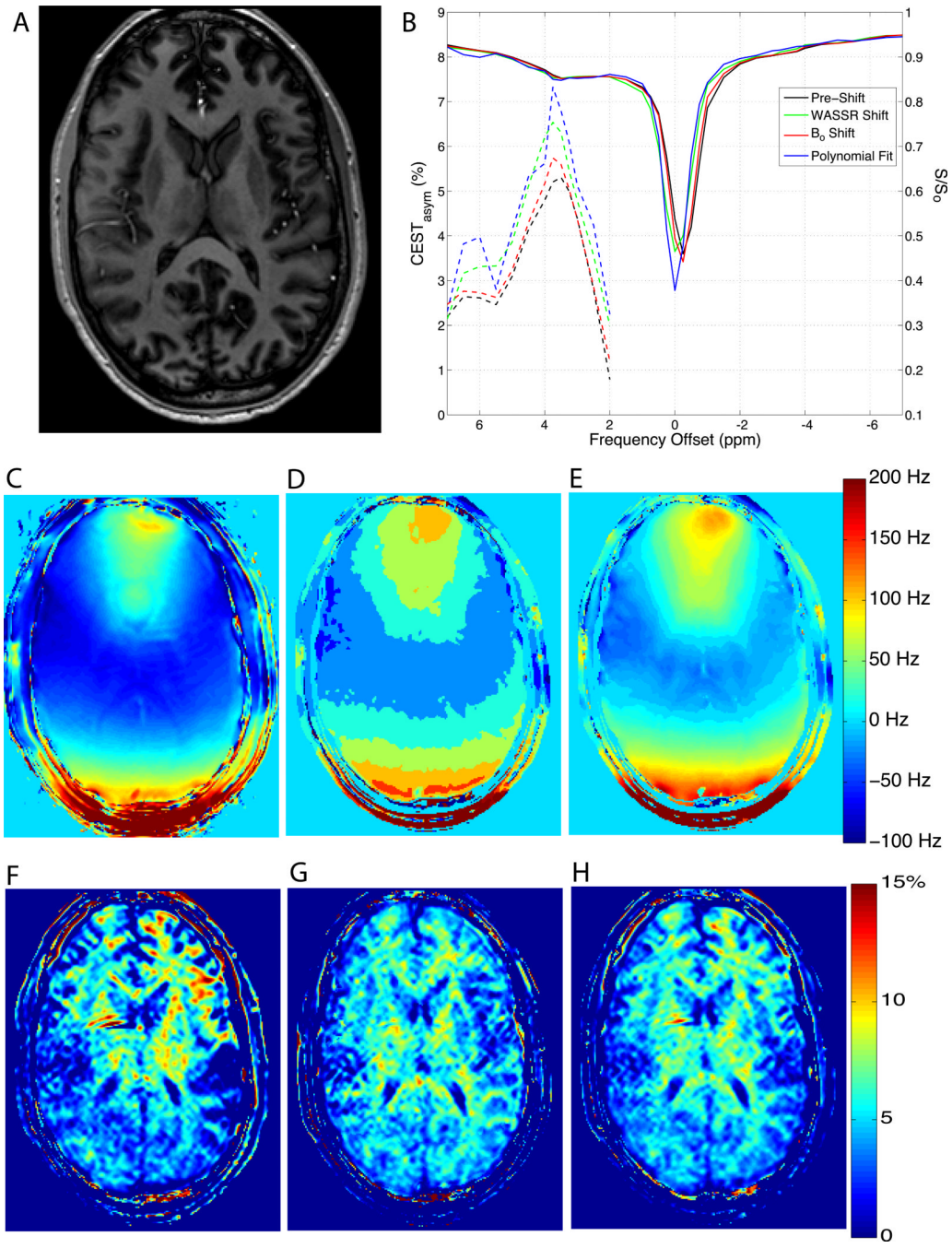

Figure 1.

Results from CEST imaging at 7T. A) CEST cpsectra from a normalized and smoothed region in the occipital white matter (solid lines, right y-axis) calculated CEST asymmetry is also shown (dashed lines, left y-axis). B) CEST spectra from a normalized and smoothed white matter region of interest (solid lines) with y-axis displayed on the right. CEST asymmetry is also shown (dashed lines) corresponding to the left y-axis. C) ΔB0 map, D) polynomial shift map, E) WASSR shift map calculated using maximum symmetry algorithm, color scale indicated on E. Asymmetry maps for the ΔB0 map (F), polynomial fit (G), and WASSR shift methods (H).

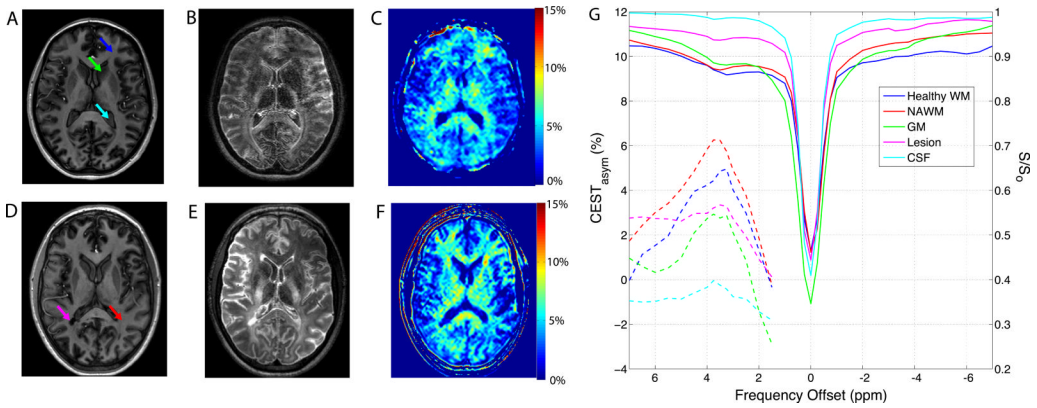

Figure 2.

7 Tesla imaging and CEST asymmetry results from a healthy control (A-C) and an MS subject (D-E). Anatomical image of healthy control (A) and MS subject (D) with ROIs indicated by arrows. T_2w FLAIR image of healthy control (B) and MS subject (E) provide alternate contrast for ROI delineation. Part G shows the normalized and shifted CEST spectra (solid lines) and asymmetry analysis (dashed lines) from various ROIs (as indicated with arrows on anatomical images A & D).

NIH-PA Author Manuscript
NIH-PA Author Manuscript
NIH-PA Author Manuscript

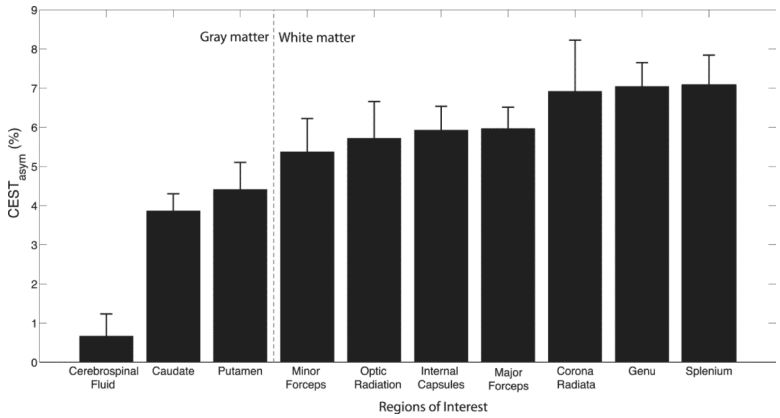

Figure 3.

Region of interest analysis of the APT_{asym} measurements at 7T from rater 1 displaying the mean with error bars indicating the standard deviation among 10 healthy controls. White matter ROIs are separated from gray matter ROIs by the gray dashed line, which demonstrates a clear delineation of this metric between the neural tissue types.

NIH-PA Author Manuscript NIH-PA Author Manuscript NIH-PA Author Manuscript

NIH-PA Author Manuscript

NIH-PA Author Manuscript

NIH-PA Author Manuscript

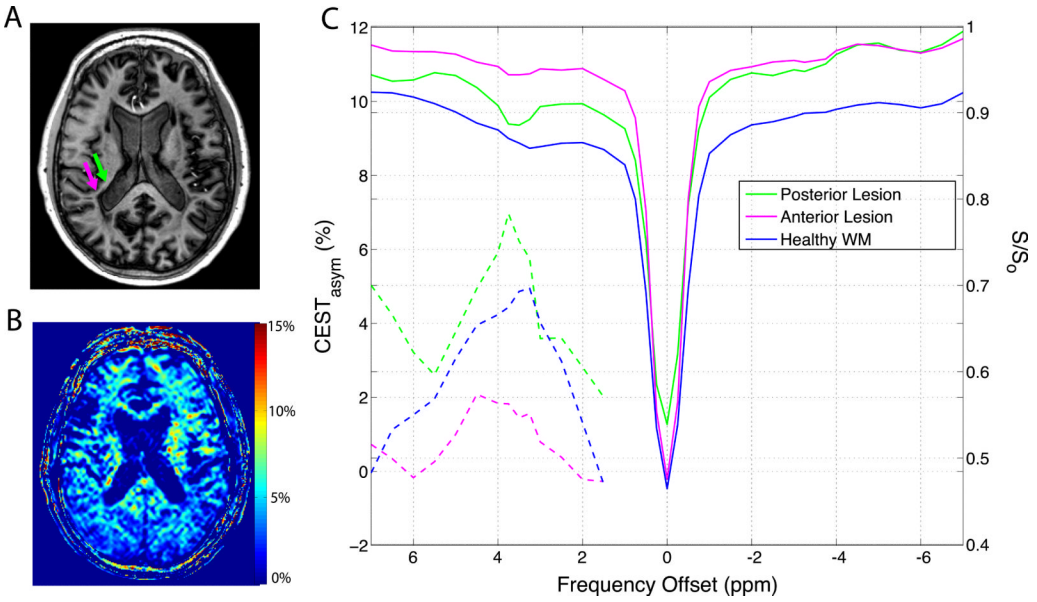

Figure 4.

Application of CEST asymmetry analysis to multiple sclerosis pathology. A) T_1-weighted anatomical image of MS patient with lesion indicated by arrows. B) APT_{asym} map calculated using CEST spectrum at 7T. C) CEST spectra (right y-axis) and $CEST_{asym}$ (left y-axis) arising from ROIs indicated on panel A revealing a heterogeneous MS lesion.

NIH-PA Author Manuscript
NIH-PA Author Manuscript
NIH-PA Author Manuscript

Table 1

7 Tesla imaging parameters.

Scan Name	TR (ms)	TE (ms)	Flip Angle (°)	Acquired Voxel size (mm)	WFS (pixels) / BW (Hz/pixel)	Other	TA (s)
Anatomical	3.7	1.98	7	1.06 × 1.05 × 3.00	1.077 / 940.8	TFE/TI = 5000/1300 ms, SENSE 2 (RL)	96.5
WASSR	40	2.4	30	2.12 × 2.12 × 6.00	0.539 / 1881.5	ND=29, RFdur/amp = 200ms/0.5uT, SENSE = 2.5 (AP)	300.9
CEST	75	2.4	30	2.12 × 2.12 × 6.00	0.539 / 1881.5	ND = 39, RFdur/amp = 1000ms/3.5uT, SENSE = 2.5 (AP)	825.3
B_0 map	48	3.9	30	2.21 × 2.25 × 6.00	2.401 / 422.0	ΔTE = 1ms	43.9

WFS = water fat shift, TFE = turbo field echo, AP = anterior/posterior, ND = number of dynamics, RFdur/amp = RF duration and amplitude

NIH-PA Author Manuscript
NIH-PA Author Manuscript
NIH-PA Author Manuscript

Table 2

Results from Bland Altman analysis for inter-rater variability of ROIs.

	Rater 1		Rater 2			Bland-Altman		t-test	
Structure	**mean ± std**		**mean ± std**		**Difference (D)**	**95% CI of mean Diff**	**LOA**	**p-value**	**DBA (%)**
Genu	7.05	0.6	6.98	0.89	0.066	(−0.2456, 0.3776)	(−0.8178, 0.9498)	0.85	0.9
Splenium	7.08	0.76	7.2	0.81	−0.123	(−0.3148, 0.0699)	(−0.6680, 0.4231)	0.73	1.7
Major Forceps	5.97	0.55	5.99	0.52	−0.022	(−0.1811, 0.1362)	(−0.4724, 0.4275)	0.93	0.4
Minor Forceps	5.38	0.85	5.48	0.84	−0.105	(−0.3901, 0.1808)	(−0.9145, 0.7052)	0.78	1.9
Optic Radiation	5.72	0.94	5.11	1.01	0.612	(0.2634, 0.9602)	(−0.3764, 1.6000)	0.18	11.3
Internal Capsules	5.93	0.61	6.16	0.82	−0.227	(−0.5509, 0.0963)	(−1.1453, 0.6906)	0.49	3.8
Corona Radiata	6.92	1.3	6.94	1.51	−0.015	(−0.2334, 0.2029)	(−0.6339, 0.6034)	0.98	0.2
Caudate	3.87	0.43	3.93	0.44	−0.058	(−0.1767, 0.0609)	(−0.3948, 0.2790)	0.77	1.5
Putamen	4.42	0.69	4.3	0.74	0.116	(−0.0691, 0.3008)	(−0.4087, 0.6405)	0.72	2.7
CSF	0.67	0.56	0.42	0.64	0.247	(−0.1527, 0.6470)	(−0.8871, 1.3814)	0.37	45.4